

Neutrino-driven explosions of ultra-stripped type Ic supernovae generating binary neutron stars

Yudai Suwa^{1,2*}, Takashi Yoshida¹, Masaru Shibata¹, Hideyuki Umeda³,
and Koh Takahashi³

¹*Yukawa Institute for Theoretical Physics, Kyoto University, Oiwake-cho, Kitashirakawa, Sakyo-ku, Kyoto, 606-8502, Japan*

²*Max-Planck-Institut für Astrophysik, Karl-Schwarzschild-Str. 1, D-85748 Garching, Germany*

³*Department of Astronomy, Graduate School of Science, University of Tokyo, Tokyo 113-0033, Japan*

Accepted. Received.

ABSTRACT

We study explosion characteristics of ultra-stripped supernovae (SNe), which are candidates of SNe generating binary neutron stars (NSs). As a first step, we perform stellar evolutionary simulations of bare carbon-oxygen cores of mass from 1.45 to 2.0 M_{\odot} until the iron cores become unstable and start collapsing. We then perform axisymmetric hydrodynamics simulations with spectral neutrino transport using these stellar evolution outcomes as initial conditions. All models exhibit successful explosions driven by neutrino heating. The diagnostic explosion energy, ejecta mass, Ni mass, and NS mass are typically $\sim 10^{50}$ erg, $\sim 0.1M_{\odot}$, $\sim 0.01M_{\odot}$, and $\approx 1.3M_{\odot}$, which are compatible with observations of rapidly-evolving and luminous transient such as SN 2005ek. We also find that the ultra-stripped SN is a candidate for producing the secondary low-mass NS in the observed compact binary NSs like PSR J0737-3039.

Key words: binaries: close — stars: evolution — stars: massive — stars: neutron — supernovae: general — supernovae: individual (SN 2005ek)

1 INTRODUCTION

Mergers of binary compact objects, i.e. neutron stars (NSs) and black holes (BHs), are promising candidates of strong gravitational wave (GW) sources. Event rates of these mergers are estimated based on the number of observed binary NSs in our galaxy and population synthesis calculations (e.g., [Abadie et al. 2010](#)). These estimates, however, have large uncertainty with, roughly speaking, two orders of magnitude. Recalling that the compact objects are formed through gravitational collapse and subsequent supernova (SN) explosions, there should be transient events generating binary compact objects observable by electromagnetic waves. SN surveys by currently working facilities e.g., The Subaru Hyper Suprime-Cam (HSC; [Miyazaki et al. 2012](#); [Tominaga et al. 2014](#)), Palomar Transient Factory (PTF; [Rau et al. 2009](#); [Law et al. 2009](#)), Catalina Real-Time Sky Survey (CRTS; [Drake et al. 2009](#)), Panoramic Survey Telescope & Rapid Response System (Pan-STARRS1; [Kaiser et al. 2010](#)), and SkyMapper ([Keller et al. 2007](#)), and also by coming future projects (e.g., Large Synoptic Survey Telescope¹; LSST) will be able to

give constraints on the formation rate of transient objects including binary compact objects.

One of the possible candidates for a SN forming a close binary system is *ultra-stripped* SN ([Tauris et al. 2015](#)), which would launch peculiar type Ib/c SN with a faint and fast decaying light curve. Peak luminosity of Type Ib/c SNe is determined primarily by the ejected mass of ^{56}Ni , $M_{56\text{Ni}}$, while the timescale around the peak is determined by the diffusion timescale $\tau_c \propto M_{\text{ej}}^{3/4} E_K^{-1/4}$, where M_{ej} is the ejecta mass and E_K is the kinetic energy of the ejecta ([Arnett 1982](#)). Therefore, the low peak luminosity and short characteristic time imply the small masses of the ejecta and ^{56}Ni . For instance, type Ic SN 2005ek is one of these SNe ([Drout et al. 2013](#); [Tauris et al. 2013](#)), whose estimated ejecta mass, $\sim O(0.1)M_{\odot}$ is notably smaller than typical SN Ic, $O(1)M_{\odot}$ ([Drout et al. 2011](#)), as well as smaller ^{56}Ni mass, and the explosion energy is also smaller by an order of magnitude ($O(10^{50})$ erg) than typical core-collapse SNe ($O(10^{51})$ erg). To model these rapidly-evolving SNe with small ejecta mass, the progenitor stars are thought to be stripped much more than canonical stripped-envelope type Ib/c SNe, that is, ultra-stripped SNe coined by [Tauris et al. \(2013\)](#); [Tauris et al. \(2015\)](#). Besides SN 2005ek and other known SNe, ten rapidly-evolving transients were recently detected by Pan-STARRS1, which exhibit shorter decay-

* E-mail: suwa@yukawa.kyoto-u.ac.jp

¹ <http://www.lsst.org/lsst/>

ing timescale (~ 10 days) than canonical SNe with peak barometric luminosities ranging from $\sim 10^{42}$ to 10^{43} erg s $^{-1}$ (Drout et al. 2014). These ultra-stripped SNe are conjectured as products of close binary systems that experienced strong binary interactions, e.g. common envelope phase, which result in close binary compact objects. Therefore, by assuming that the order of the ultra-stripped SN rate is the same as that of the merger rate, we will be able to measure the merger rate through SN surveys. The current predictions of NS merger rate is between $\sim 10^{-6}$ and 4×10^{-3} galaxy $^{-1}$ year $^{-1}$ (Abadie et al. 2010), which are corresponding to $\sim 0.01\%$ and 40% of core-collapse SN rate (~ 0.01 galaxy $^{-1}$ year $^{-1}$), while observed ultra-stripped SN rate would be $\sim 0.1\text{--}1\%$ of supernovae (Tauris et al. 2015). After the detection of GWs, this conjecture can be tested using statistics of GW sources.

To predict the properties of these transient objects for coming LSST era, we investigate the explosion characteristics of the ultra-stripped SNe by means of numerical simulations. The current standard model of the explosion mechanism for core-collapse SNe is based on a neutrino-driven delayed explosion scenario (Colgate & White 1966; Bethe & Wilson 1985), in which copious amount of neutrinos emitted in the vicinity of a newly-born NS are absorbed by the surrounding materials and they effectively act as heating (see Janka 2012; Kotake et al. 2012; Burrows 2013; Foglizzo et al. 2015, for latest reviews and references therein). In this study, we perform i) stellar evolutionary simulations of bare carbon and oxygen (CO) cores without massive hydrogen and helium envelopes, which would be possible consequences of close binary interactions such as common envelope phase, until iron cores form and ii) axisymmetric neutrino-radiation hydrodynamics simulations to investigate their explosions. The paper is organized as follows. Section 2 describes our stellar evolutionary simulations and stellar structure just prior to the collapse. The numerical method of following hydrodynamics simulations and the results are presented in Section 3. We summarize our results and discuss their implications in Section 4.

2 STELLAR EVOLUTION AND PROGENITOR STRUCTURES

Here, we describe the evolution of CO cores obtained in this study. To make initial conditions for hydrodynamics simulations, we first perform stellar evolutionary simulations of CO cores with masses of 1.45, 1.5, 1.6, 1.8, and $2.0 M_{\odot}$ supposing that stellar mass loss has already occurred by their hypothetical companion NSs. By removing stellar envelope, the stellar evolutionary simulations are done with a code described in Umeda et al. (2012); Takahashi et al. (2013); Yoshida et al. (2014). The nuclear reaction network consists of 300 species of nuclei (Takahashi et al. 2013; Yoshida et al. 2014). Schwarzschild criterion is employed as the convection criterion and the convective mixing of the chemical composition is evolved using diffusion equation. We also take into account thermohaline mixing (e.g. Siess 2009) and the diffusion coefficient is adopted from Eq. (2) in Siess (2009). The initial chemical compositions of the CO cores are evaluated by those after the He burning with the metallicity $Z = 0.02$. Since the C/O ratio of the core depends on the stellar mass,

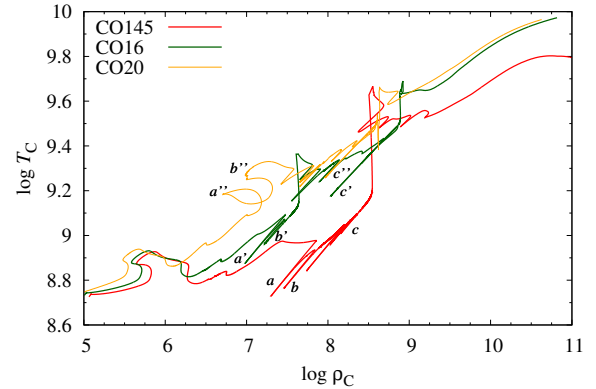


Figure 1. Evolutionary path in the plane of the central density and temperature of CO145 (red line), CO16 (green line), and CO20 (orange line) models. Labels a and a' , b and b' , and c , c' , and c'' correspond to the off-center Ne, O, and Si burnings, respectively. Labels a'' and b'' denote the central Ne and O burnings.

we assume the mass fractions of ^{12}C and ^{16}O , which are listed in Table 1.

It is quite difficult to relate between ZAMS mass and CO-core mass in binary systems because mass transfer proceeds very complicatedly during the evolution. On He star-NS binaries, He stars with $M_{\text{He}} \lesssim 3.5 M_{\odot}$ and with the initial orbital period of $P_{\text{orb}} \lesssim 0.5\text{d}$ have an evolutionary path to ultra-stripped SNe (Tauris et al. 2015). These He stars evolved to CO cores with $M_{\text{CO}} \lesssim 1.8 M_{\odot}$ surrounded by very thin He envelope. Thus, the mass range of our CO core models is adequate for the progenitors of ultra-stripped SNe. For comparison, we list the stellar mass at the zero-age main-sequence (ZAMS), M_{ZAMS} , which makes the similar CO core as shown in Table 1. The mass range of the He cores is $2.6 - 3.3 M_{\odot}$. These values are evaluated based on the evolution of $9 - 15 M_{\odot}$ stars up to the Ne ignition or the central C exhaustion (see also Woosley & Heger 2015). We assume the convective overshooting as a diffusion process until the core He burning in these calculations. The diffusion coefficient is adopted from Eq. (2) in Herwig (2000) and the parameter on the scale height f is set to be 0.01.

We continue evolutionary simulations until the iron cores become unstable and start collapsing. Here we briefly explain the evolution of our models. More details will be shown in Yoshida et al. (2015, in preparation). Figure 1 shows the evolution of the central temperature (T_c) and density (ρ_c) of CO145, CO16, and CO20 models. Here, the units of T_c and ρ_c are Kelvin and g cm $^{-3}$, respectively. Figure 2 is the Kippenhahn diagram of CO145 model, which displays the time evolution of convective regions and the energy generation inside the star. Although all models finally form Fe cores, the evolution paths depend on the CO-core mass. In CO145 model, off-center Ne burning is ignited (Ne-flash) after several C-shell burnings (label a in Figures 1 and 2). The following O-burning is also ignited at an off-center region (label b). Then, the burning front gradually moves into the center and the temperature at the front increases. When the central density reaches $\log \rho_c \sim 8.2$, Si-burning is ignited at the burning front and the convective layer extends to $M_r \sim 0.9 M_{\odot}$ (label c). The burning front continues

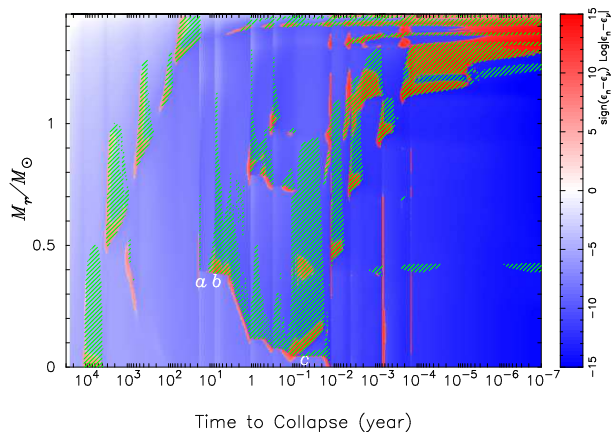


Figure 2. Kippenhahn diagram of CO145 model. Green-hatched areas indicate convective regions. Labels *a*, *b*, and *c* correspond to the off-center Ne, O, and Si-burnings at 17.1 years, 10.7 years, and 38.8 days before core-collapse.

to move inwards and the O/Ne-enriched material in the central region is burned to Fe-peak elements. When the central density reaches $\log \rho_C \sim 8.5$, the burning front reaches the center and the central temperature raises steeply. The Fe core grows up to $\sim 0.5 M_\odot$ after the burning front reaches the center. Then, shell Si-burning occurs and the Fe core grows up further, and finally, the core collapses.

CO16 model evolves on a different evolution track as shown in Figure 1. After the Ne flash (label *a'*) and off-center O burning (label *b'*), the burning front reaches the center. As a result, the Si core with $0.6 M_\odot$ is formed and it grows up by O-shell burnings. Then, the Si flash occurs at $M_r = 0.03 M_\odot$ (label *c'*). The Si flash forms large convective region up to $M_r \sim 1.1 M_\odot$ above the burning front. After that, Si-shell burnings also follow. The burning front again gradually moves inwards and finally reaches the center after the second Si-shell burning. Finally, the Fe core grows to $1.34 M_\odot$ and collapses. The evolution of CO15 model is similar to that of CO16. The Ne-flash and Si-flash occur at higher central density.

The evolution of CO20 model is similar to those of massive stars that collapse to normal SNe until O-shell burning. Ne and O burnings are ignited at the center and the convective core forms (labels *a''* and *b''*). The Ne and O-shell burnings extend the central Si core after O-core burning. However, Si burning starts at an off-center region when the central density reaches $\log \rho_C \sim 8.6$ (label *c''*). The off-center Si burning forms a large convective region to $1.2 M_\odot$. The burning front moves inwards and reaches the center during Si-shell burning. Finally, an $1.37 M_\odot$ Fe core is formed, and then, it collapses. The evolution of CO18 model is similar to CO20 model, i.e., Ne and O are ignited at the center and Si ignites at an off-center region. The central density at the ignition of off-center Si-burning is higher than that of CO20.

We note that recently the evolution of 9 - 11 M_\odot stars has been investigated in Woosley & Heger (2015). Since they considered artificial energy deposition to the cooler underlying zone of the off-center burning front, the burning front rapidly moved inward. We do not consider this effect, but we instead set larger coefficient value of thermohaline mixing. In CO145 model, the central contraction makes the temper-

ature at the burning front high enough to ignite Si before the front reaches the center. Even so, CO145 model forms an Fe core. Although the inward motion of the burning front depends on the instability at the base of the burning front and has uncertainty, we expect that the stars igniting Ne-flash will form an Fe core and collapse.

The mass fraction distributions of CO145 and CO16 models at the final step of the stellar evolution simulations are shown in Figure 3. These models consist of a 1.33 and 1.34 M_\odot Fe cores surrounded by thin Si, O/Si, O/Ne, and O/C layers. Composition-inverted layers have been seen during the Ne-flash and Si flash. The composition inversion has been removed during the inward motion of the burning front. We do not see large differences in Fe core masses in our CO core models (see Table 1).

We assume the mass fractions of C and O in the CO cores based on the results of single star models. In the case of binary evolution, ultra-stripped CO cores have lost the H-rich envelope before or during the early phase of the He-core burning. Stripping the H-rich envelope prevents the growth of He core and shortens the time scale of the He-core burning. Thus, the C/O ratio of an ultra-stripped CO core is larger than the CO core in single stars (Brown et al. 2001). Wellstein & Langer (1999) investigated the evolution of various binary systems of massive stars. They obtained that a binary system consisting of 13 M_\odot and 12 M_\odot stars with an initial orbital period of 3.1 days experiences Case B+BB mass transfer and the primary star becomes a 1.42 M_\odot He star with CO core mass being 1.31 M_\odot and the central carbon mass fraction being 0.40.

We calculate the evolution of 1.45 and 1.6 M_\odot CO core models with a large C/O ratio to investigate the C/O-ratio dependence of ultra-stripped SN progenitors. We set the mass fractions of C and O in these models to be 0.471 and 0.500, respectively. Properties of the models are shown as CO145c and CO16c in Table 1. We do not see large systematic differences between normal and large C/O-ratio models. CO145c model has an Fe core slightly smaller than CO145, while the Fe core of CO16c is slightly larger than that of CO16 for the criterion that the Fe core is determined by the electron fraction smaller than 0.495. The difference of the compactness parameter between the normal model and large C/O-ratio model is within 10 %. We consider that properties of ultra-stripped SN progenitor do not strongly depend on the C/O ratio. It should be noted that the evolution of the central region of the CO cores depends on the C/O ratio. The convective regions of the central or shell C-burnings become large in the models of the large C/O ratio. In CO145c model, Ne is ignited at 0.35 M_\odot in the mass coordinates. The Ne/O-burning front reaches the center before the Si ignition. Then, Si is ignited at 0.04 M_\odot . In CO16c model, Si-burning occurs at the center as a flash and, then, it turns to steady burning. Nevertheless, we do not see large difference by the C/O ratio in the region where the structures and composition are mainly determined by the Si-shell burning. Once the Fe core is formed by the central or off-center Si-burning, the core grows through the following Si-shell burning. Thus, we consider that properties of SN progenitors such as Fe core mass and compactness parameter are insensitive to the C/O ratio.

These CO cores have a thin CO envelope where shell C burnings scarcely affect the composition. We listed the

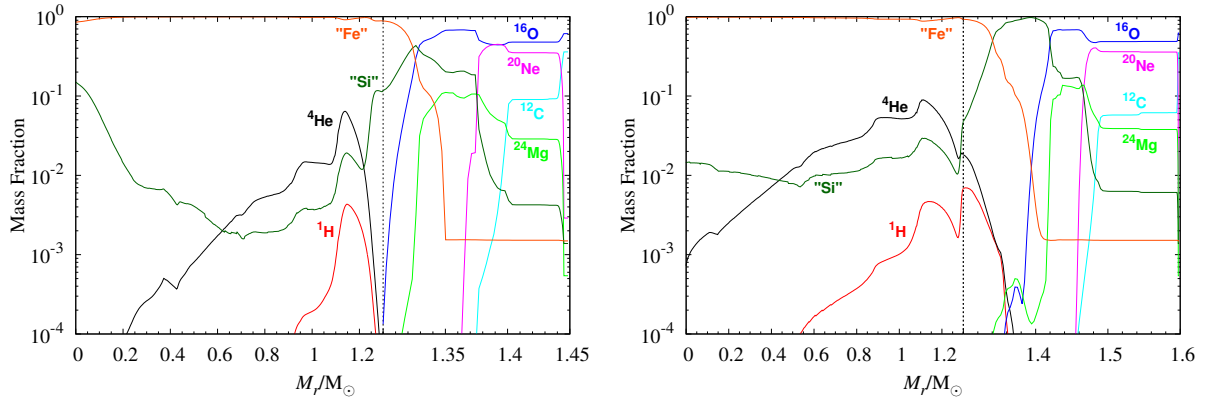


Figure 3. Mass fraction distributions of CO145 (left) and CO16 (right) models. Red, black, sky-blue, blue, pink, yellow-green, green, and orange lines correspond to ^1H , ^4He , ^{12}C , ^{16}O , ^{20}Ne , ^{24}Mg , “Si”, and “Fe”. “Si” and “Fe” indicate the element groups in $Z = 14 - 21$ (Si-Sc) and $Z \geq 22$ (Ti-), respectively. The scale of the horizontal axis changes at $1.3 M_\odot$.

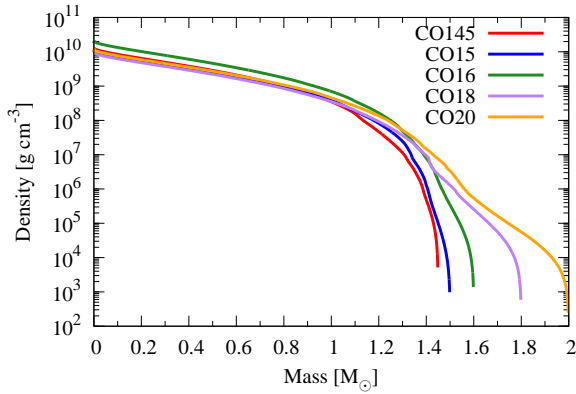


Figure 4. Density structure of CO cores at precollapse phase as a function of mass coordinate. Red, blue, green, purple, and orange lines represent models with CO cores of 1.45 , 1.5 , 1.6 , 1.8 , and $2.0 M_\odot$, respectively.

masses of the envelope, M_{env} , which the convective region did not reach during C-shell burnings, and their binding energy, $E_{\text{bind,env}}$, in Table 1. The envelope mass is less than $0.01 M_\odot$ for all the models. The binding energy of the envelope is $(0.4 - 2) \times 10^{48}$ erg, which is smaller than one per cent of the binding energy of the whole star (E_{bind} , see Table 1).

Although we do not take into account He-rich envelope, the progenitors of ultra-stripped SNe in NS binary systems could have the envelope (Tauris et al. 2013; Tauris et al. 2015). Tauris et al. (2015) showed the dependence of the He mass and the binding energy of the He-envelope on the final CO core mass. Here, we estimate the binding energy of the He-envelope from Figure 15 in Tauris et al. (2015) and from their discussion that the He mass is smaller than $0.2 M_\odot$ (see §4.1.1 in Tauris et al. 2015). The estimated range of the envelope is listed in Table 1. The binding energy of the He envelope is at most several times 10^{49} erg. Thus, we expect that the envelope has a small contribution in the binding energy for ultra-stripped SNe.

Figure 4 presents density structures at the end of evolutionary simulations. More detailed properties are summarized in Table 1. Following O’Connor & Ott (2011), we de-

fine the compactness parameter, ξ_M , by

$$\xi_M = \frac{M/M_\odot}{R(M)/1000 \text{ km}}, \quad (1)$$

where $R(M)$ is the radius with M being mass enclosed inside R . We employ $\xi_{1.4}$, which is measured by $M_r = 1.4 M_\odot$. Note that other groups have employed different values such as $\xi_{2.5}$, $\xi_{1.75}$, $\xi_{1.5}$ (O’Connor & Ott 2011; Ugliano et al. 2012; O’Connor & Ott 2013; Sukhbold & Woosley 2014; Nakamura et al. 2014; Pejcha & Thompson 2015). Since our models have small CO core mass, we rely on a different parameter. Note also that in the original definition by O’Connor & Ott (2011), ξ is measured at the time of bounce. Later, Sukhbold & Woosley (2014) suggested that ξ measured just prior to collapse correlates with ξ at bounce. Hence, in this paper we evaluate ξ with the precollapse density structures. We show two different definitions of the iron core mass, M_{Fe} : one is based on the electron fraction and the other on mass fraction of heavy elements. The iron core mass does not depend strongly on CO core mass since, broadly speaking, the core collapse sets in when the iron core mass exceeds Chandrasekhar mass (Baron & Cooperstein 1990).

3 HYDRODYNAMICS SIMULATIONS

3.1 Numerical methods

For the hydrodynamics simulations, we employ a two-dimensional (2D) neutrino-radiation hydrodynamics code, which is developed and used for investigating SN explosion mechanism (Suwa et al. 2010, 2011, 2013; Suwa et al. 2014; Suwa 2014). With ZEUS-2D code (Stone & Norman 1992) as a base for the solver of hydrodynamics, we employ an equation of state of Lattimer & Swesty (1991) with an incompressibility $K = 220$ MeV and solve the spectral transfer of neutrinos by the isotropic diffusion source approximation (IDSA) scheme (Liebendörfer et al. 2009) that splits the neutrino distribution function into two components, both of which are solved by using separate numerical techniques. Weak interaction rates are implemented following Bruenn (1985). We solve transfer of electron-type neutrinos (ν_e) and antineutrinos ($\bar{\nu}_e$), but heavier leptonic neu-

Table 1. Properties of progenitor models

Model	M_{CO} [M_{\odot}]	M_{ZAMS}^a [M_{\odot}]	X_{C}	X_{O}	Radius [10^4 km]	$\xi_{1.4}$	M_{Fe}^b [M_{\odot}]	M_{Fe}^c [M_{\odot}]	M_{env} [$10^{-3} M_{\odot}$]	$E_{\text{bind,env}}$ [10^{48} erg]	$E_{\text{bind,He}}^d$ [10^{49} erg]	E_{bind} [10^{50} erg]
CO145	1.45	9.75	0.360	0.611	1.28	0.468	1.33	1.32	4.80	2.28	0.1–1.3	3.97
CO145c	1.45	9.75	0.471	0.500	1.78	0.502	1.31	1.28	1.45	0.46	0.1–1.3	3.99
CO15	1.5	10.0	0.360	0.611	2.20	0.600	1.31	1.29	1.60	0.38	0.5–1.7	4.17
CO16	1.6	10.5	0.350	0.621	1.93	0.912	1.34	1.34	2.63	0.80	0.7–2.8	5.39
CO16c	1.6	10.5	0.471	0.500	1.73	0.850	1.36	1.34	2.42	0.95	0.7–2.8	4.69
CO18	1.8	11.5	0.350	0.621	2.64	0.851	1.35	1.37	8.09	2.20	1.2–3.8	4.92
CO20	2.0	12.8	0.330	0.641	3.66	0.968	1.37	1.37	8.48	1.66	2.2–4.7	5.72

^a This is corresponding mass of ZAMS stars, which make the same mass of CO core.

^b The iron core mass is determined by the mass with the electron fraction of $Y_e < 0.495$.

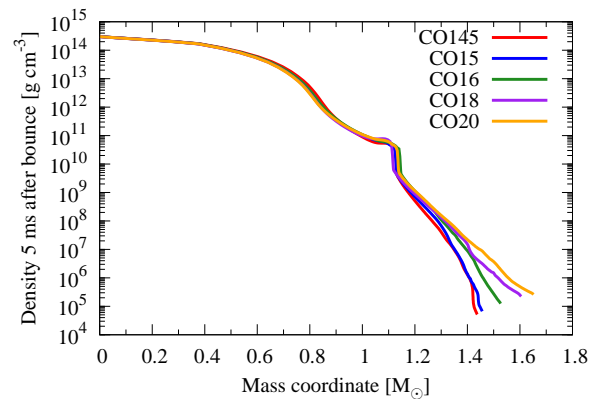
^c The iron core mass is determined by the mass with the mass fraction of the element groups in $Z \geq 22$ (Ti-) larger than 0.5.

^d These values are taken from Figure 15 in Tauris et al. (2015).

trinos are not taken into account. In our 2D simulations, axial symmetry is assumed and “ray-by-ray-plus” approach is implemented for multi-dimensional treatment of neutrino transfer (Buras et al. 2006). Spherical coordinates (r, θ) with logarithmic zoning in the radial direction and constant zoning in θ are used. The simulations are performed on a grid of 300 radial zones extending up to 5000 km with the smallest grid width being 1 km at the center and 128 equidistant angular zones covering $0 < \theta < \pi$ for 2D simulations. For neutrino transport, we use 20 logarithmically spaced energy bins ranging from 3 to 300 MeV.

Note that at the current moment there is no complete model for the explosion mechanism of core-collapse SNe despite the long-lasting efforts. Recent multi-dimensional simulations of neutrino radiation hydrodynamics have shown diversity of numerical results (e.g. Bruenn et al. 2013; Suwa et al. 2014; Dolence et al. 2015; Melson et al. 2015b, used the same progenitor models and obtained different results). In addition, most exploding simulations exhibited order of magnitude smaller explosion energy than observation and remnant compact objects often gained mass above the maximum mass of a NS, which would collapse to BHs instead of NSs.

We speculate, however, that all these implementations could universally reproduce ultra-stripped SNe. The reason for this speculation is that typical explosion energy of the ultra-stripped SNe is smaller ($O(10^{50})$ erg) than canonical SNe ($O(10^{51})$ erg), that is, stellar structures of progenitors for these different kinds of SNe are different. The explosion energy is determined naively by the binding energy of progenitor layers in the vicinity of mass cut (remnant compact object) so that stars with small binding energy are possible candidates of the weak explosions. This hypothesis was already applied for explanation of type IIIn-P SNe like SN 2009kn, which exhibit narrow emission lines, a short plateau phase in light curve, and small amount of ^{56}Ni . These observational features were reproduced by an electron-capture SN model, in which the progenitor star consists of an O-Ne-Mg degenerated core and a very thin envelope, giving the small explosion energy of $\sim 10^{50}$ erg (Moriya et al. 2014 based on the explosion simulation by Kitaura et al. 2006). As we will show in the following subsection, we obtain explosion energy of $O(10^{50})$ erg, which is the same order of magnitude as the binding energy exterior to a remnant compact object

**Figure 5.** Density profiles at 5 ms after bounce. Line colors show the same models as Figure 4.

at precollapse phase. We infer that even if we could perform a *realistic simulation* that would reproduce canonical explosion energy for canonical SN progenitors, the results obtained with weakly bound progenitors will be a weak explosion with its energy $\sim 10^{50}$ erg. Since the explosion energy of such simulations, however, could be larger than that of ours, it is safe to consider that our results give at least a lower limit of the explosion energy.

At first, we perform spherically symmetric (1D) simulations up to 5 ms after the bounce, which is determined by the largest central density, and 2D simulations follow them. Note that all 1D simulations fail to explode even when we continue simulations until several hundred milliseconds after the bounce.²

3.2 Results

We show the density profiles at 5 ms after the bounce in Figure 5. One can find that the density profiles of $M_r \lesssim 1.1M_\odot$ depend only weakly on the CO core mass, but above this mass coordinate they differ from each other due to the different progenitor structure. This difference leads to different evolution of shocks, which is described in the following. Note that the density at a certain mass coordinate above $\sim 1.1M_\odot$ monotonically increases with the CO core mass.

Figure 6 presents evolution of entropy (left halves) and radial velocity (right halves) distributions at 100 (left top panel), 200 (right top), 250 (left bottom), and 350 (right bottom) ms after the bounce for model CO15. After core bounce, convective motion sets in initially due to an unstable entropy configuration (prompt convection) and subsequently due to neutrino heating in the gain region (neutrino-driven convection), but shock morphology is maintained to be approximately spherically symmetric (see left top panel). As the turbulent motion is further enhanced by the neutrino heating, the shock is deformed from spherical symmetry (see right top). Once the postshock pressure (thermal pressure and turbulent pressure) overwhelms the ram pressure above the shock, the shock starts expanding and an explosion is launched. In this model, the expanding shock is rather spherical since the small envelope mass results in a small mass accretion rate onto the shock and small-scale convection dominates over large-scale motion driven by the standing accretion shock instability (SASI; Blondin et al. 2003). This leads to a small kick velocity of protoneutron stars (PNS). One can observe a cold downflow onto the PNS even after the onset of the explosion (see an isolated blue region in the bottom right panel of Figure 6), which could increase the PNS mass. This downflow, however, has a small solid angle and the mass accretion rate is considerably small. Thus, the mass accreting onto the PNS at this moment is negligible. The PNS mass evolution will be discussed later.

Shock evolution processes in all 2D simulations are presented in Figure 7. One can see that the three small mass models (CO145, CO15, and CO16) explode approximately at identical time, while more massive cores show later explosion. This is a consequence of the different envelope mass on the iron core. The early exploding models have clear phase transition from a slowly expanding phase to a rapidly exploding phase at ~ 200 ms after the bounce. On the other hand, late exploding models show oscillations of the shock radius before the explosion. This is due to convection and SASI. The difference in the onset time of the explosion is a result of different mass accretion rate evolution due to the different envelope structure (see Figure 5). The later onset of the explosion leads to larger PNS mass as shown in Figure 8. Here we define PNS as the region with density above 10^{11} g cm $^{-3}$. CO145 and CO15 models form a PNS of baryonic mass $\approx 1.35M_\odot$, while other models give larger PNS mass.

In Table 2, we summarize results of our hydrodynamics

simulations. t_{final} denotes the final postbounce time of each simulation. The quantities listed in other columns are all measured at t_{final} . R_{sh} is the angle-averaged shock radius, E_{exp} is diagnostic explosion energy, which is defined as the integral of the sum of specific internal, kinetic and gravitational energies over all zones with positive value, $M_{\text{NS,baryon}}$ is baryonic mass of the remnant NS calculated by integration over grid of $\rho > 10^{11}$ g cm $^{-3}$, $M_{\text{NS,grav}}$ is the corresponding gravitational mass, $M_{\text{ej}} = M_{\text{CO}} - M_{\text{NS,baryon}}$ is the ejecta mass, $M_{56\text{Ni}}$ is mass of ^{56}Ni , and v_{kick} is the estimated kick velocity of NSs. Note that these quantities are not the final outcome of the simulations, since all the simulations were terminated before the system relaxes to a stationary state to save the computational time. The gravitational mass is calculated by the baryonic mass using the following relation (Timmes et al. 1996)

$$\frac{M_{\text{baryon}}}{M_\odot} - \frac{M_{\text{grav}}}{M_\odot} = 0.075 \left(\frac{M_{\text{grav}}}{M_\odot} \right)^2. \quad (2)$$

^{56}Ni mass is calculated using tracer particle method (e.g., Nagataki et al. 1997). We assume that the mass elements with the maximum temperature being over 5×10^9 K achieve nuclear statistical equilibrium and synthesize ^{56}Ni completely. This gives just an approximate estimate. For more realistic calculation we need to perform detailed nucleosynthesis calculation, which is beyond the scope of this paper. The NS kick velocity is estimated by assuming the linear momentum conservation of the whole progenitor star, i.e., assuming that anisotropic mass ejection leads to NS kick (e.g., Wongwathanarat et al. 2013). The linear moment of ejecta is calculated by

$$\mathbf{P}_{\text{ej}} = \int_{\rho < 10^{11} \text{ g cm}^{-3}, v_r > 0} \rho \mathbf{v} dV, \quad (3)$$

where \mathbf{v} is the velocity vector and v_r is its radial component. The NS kick velocity is then given by $\mathbf{v}_{\text{kick}} = -\mathbf{P}_{\text{ej}}/M_{\text{NS,baryon}}$. Since the axial symmetry is assumed in our simulations, the kick velocity may be overestimated due to the existence of preferable direction of NS kick, i.e. symmetry axis. Additionally, the stochastic nature of postshock turbulent flow would also change the degree of asymmetry of ejecta so that the the initial small perturbation could change the kick velocity significantly (Scheck et al. 2006). More statistical study is needed to pin down this issue. It can be argued that small envelope, not small iron core itself, which can rapidly accelerate shock, would generally lead to small kick velocity due to too short time for SASI to build up (see also, e.g., Podsiadlowski et al. 2004; Bogomazov et al. 2007).

4 SUMMARY AND DISCUSSION

We have performed both stellar evolution simulations of bare CO cores and explosion simulations for the end product of the CO cores for modeling ultra-stripped type Ic SNe. We have found that all CO cores with mass from 1.45 to 2.0 M_\odot resulted in explosion with energy of $O(10^{50})$ erg, which left NSs with gravitational mass from ~ 1.24 to 1.44 M_\odot and ejecta from ~ 0.1 to 0.4 M_\odot with synthesized ^{56}Ni of $O(10^{-2})M_\odot$. These values are compatible with observations of ultra-stripped SN candidates (Drouot et al. 2013;

² Note that recent studies of full three-dimensional (3D) hydrodynamics simulations showed that 2D simulations are more favorable for explosion than those of 3D (see e.g., Hanke et al. 2013; Takiwaki et al. 2014) so that we should note that the 2D simulations would optimize the conditions for successful explosions (but see also Melson et al. 2015a).

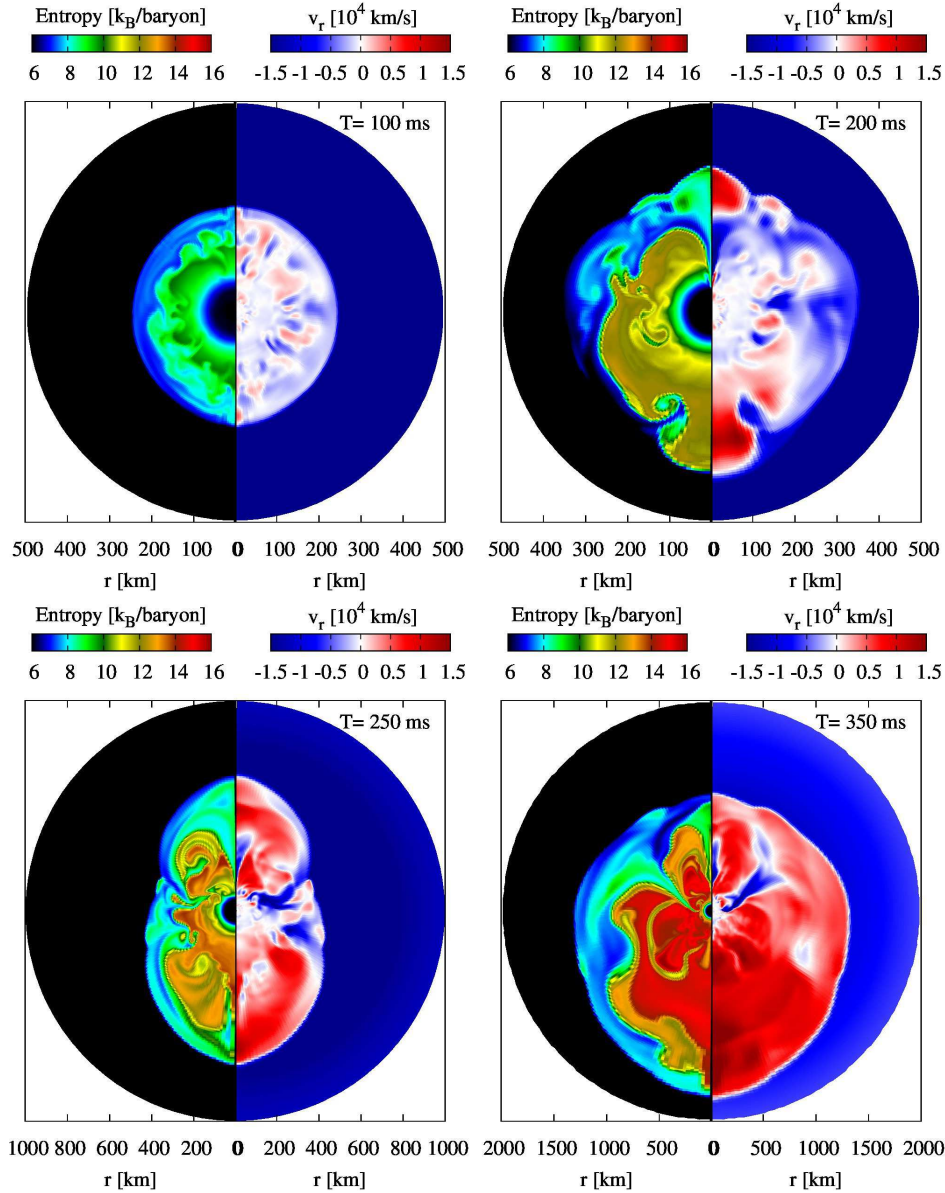


Figure 6. Specific entropy (in unit of k_B baryon $^{-1}$; left halves of the individual panels) and radial velocity (in unit of 10^4 km s $^{-1}$; right halves) profiles at 100 (left top panel), 200 (right top), 250 (left bottom), and 350 (right bottom) ms after the bounce for model CO15. In the entropy plots, blueish (reddish) colors represent small (large) entropy. In velocity plots, red region is expanding (positive radial velocity) and blue region is accreting (negative radial velocity).

Tauris et al. 2013; Tauris et al. 2015). For SN 2005ek, $M_{\text{ej}} \approx 0.2\text{--}0.7 M_\odot$ and $M_{\text{Ni}} \approx 0.02\text{--}0.05 M_\odot$ are appropriate to fit its light curve. The event rate of these SNe is estimated as $\sim 1\%$ of core-collapse SN rate (Drout et al. 2013, 2014), which is also compatible with an NS merger rate estimation (Abadie et al. 2010).

We took a different approach from previous studies on ultra-stripped SNe (Tauris et al. 2013; Tauris et al. 2015). In previous works, they self-consistently performed stellar evolutionary simulations until oxygen burning phase with self-consistent mass loss driven by wind but explosion calculations were based on phenomenological modeling with three free parameters; kinetic energy of SN, Ni mass, and mass cut (i.e. NS mass). Based on this model, they found that ultra-stripped SN model could account for the light curve of SN

2005ek quite well. In our work, on the other hand, we performed stellar evolutionary simulations until the last phase of evolution, i.e., iron core collapse, but for initially bare CO cores without mass loss. For the explosion phase, we performed neutrino radiation hydrodynamics simulations to calculate explosion energy, Ni mass, and NS baryon mass in self-consistent manner. In this sense, this work is complementary to previous works. We found that outcomes of our hydrodynamics simulations for CO145, CO15, and CO16 are close to model parameters of Tauris et al. (2013) that well fit light curve of SN 2005ek ($M_{\text{NS}} = 1.3M_\odot$, $M_{\text{ej}} = 0.2M_\odot$, $E_{\text{exp}} = 5 \times 10^{50}$ erg, and $M_{\text{Ni}} = 0.05M_\odot$). The light curve calculated with our hydrodynamical models will be presented in the forthcoming paper.

For CO145, CO15, CO16, and CO18 models, the baryon

Table 2. Summary of simulation results

Model	t_{final}^a [ms]	R_{sh}^b [km]	E_{exp}^c [B]	$M_{\text{NS,baryon}}^d$ [M_{\odot}]	$M_{\text{NS,grav}}^e$ [M_{\odot}]	M_{ej}^f [$10^{-1} M_{\odot}$]	M_{Ni}^g [$10^{-2} M_{\odot}$]	v_{kick}^h [km s $^{-1}$]
CO145	491	4220	0.177	1.35	1.24	0.973	3.54	3.20
CO15	584	4640	0.153	1.36	1.24	1.36	3.39	75.1
CO16	578	3430	0.124	1.42	1.29	1.76	2.90	47.6
CO18	784	2230	0.120	1.49	1.35	3.07	2.56	36.7
CO20 ⁱ	959	1050	0.0524	1.60	1.44	3.95	0.782	10.5

^a The final time of simulations measured by postbounce time.

^b The angle-averaged shock radius at t_{final} .

^c The explosion energy in unit of B ($=10^{51}$ erg) at t_{final} , which is still increasing.

^d The baryonic mass of NS at t_{final} .

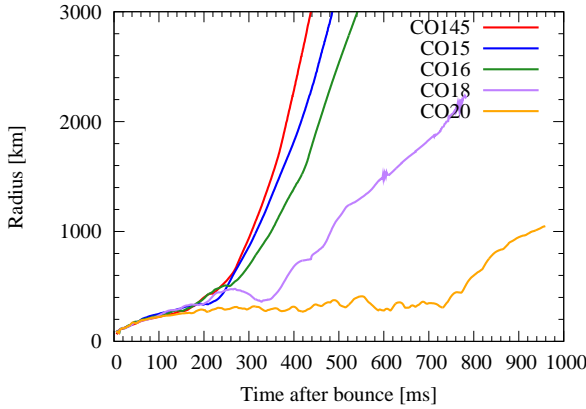
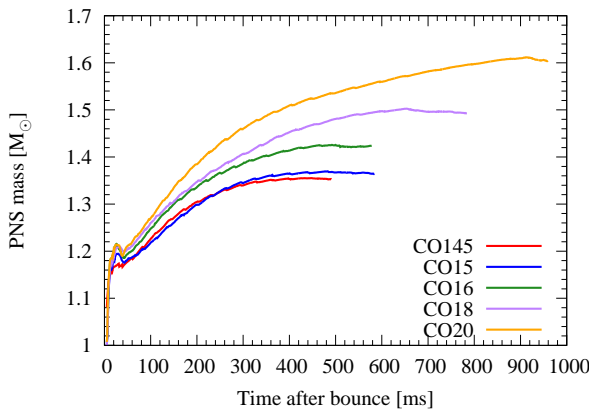
^e The gravitational mass of NS computed by Eq. (2) at t_{final} .

^f The ejecta mass at t_{final} .

^g The Ni mass at t_{final} .

^h The kick velocity at t_{final} .

ⁱ Note that this model is marginally exploding.

**Figure 7.** Evolutions of the radius of shocks.**Figure 8.** Time evolutions of PNS mass (define by $\rho > 10^{11}$ g cm $^{-3}$).

mass of the remnant NSs is in the range between $1.35M_{\odot}$ and $1.49M_{\odot}$. The corresponding gravitational mass are 1.24 - $1.35M_{\odot}$ for this baryon mass range depending only weakly on equations of state for neutron stars hypothetically employed. These values for the gravitational mass agree well

with those for secondary NSs in observed compact binary systems (Lattimer 2012). This suggests that such secondary NSs may be formed from ultra-stripped SNe.

We showed that $1.45 - 2.0M_{\odot}$ CO star models ignite Ne at the center or an off-center region. They form an Fe core and none of them evolve to electron-capture SN. Thus, the upper-limit of the CO core mass for electron-capture SN should be less than $1.45 M_{\odot}$. Tauris et al. (2015) adopted $M_{\text{ONe,f}} = 1.43M_{\odot}$ as an approximate upper limit for electron-capture SN. In the case of single star evolution in Takahashi et al. (2013), a $10.8 M_{\odot}$ model ends its evolution as an electron-capture SN and an $11.0 M_{\odot}$ model ignites Ne at an off-center region. Off-center Ne ignition and gradual increase in the central temperature around the central density $\rho_{\text{C}} \sim 10^9$ g cm $^{-3}$ could be predictions of the Fe core formation and core-collapse SN. The evolution of CO cores less massive than $1.45 M_{\odot}$ will be shown in the forthcoming paper (Yoshida et al. 2015, in preparation).

Finally, we discuss the eccentricity of the binary system formed after the SN that leaves a secondary NS. Due to the mass ejection from the system, the binary system obtains the eccentricity, e , after the SN explosion. The eccentricity can be evaluated by (Bhattacharya & van den Heuvel 1991)

$$e = \frac{M_1^i - M_1^f}{M_1^f + M_{\text{NS}}}, \quad (4)$$

where M_1 is the mass of exploding star before (after) the explosion indicated as i (f) and M_{NS} is the mass of the primary NS. Here, we assumed that the mass ejection occurs quickly and during the explosion the positions of these stars do not change. By giving the ejected mass, $M_{\text{ej}} = M_1^i - M_1^f = 0.3M_{\odot}$ and $M_1^f = M_{\text{NS}} = 1.3M_{\odot}$, we get $e \approx 0.12$, which is compatible with one of observed binary NSs, J0737-3039, whose current eccentricity is 0.088 and estimated eccentricity at birth of second pulsar is 0.11 (Piran & Shaviv 2005). The small center of mass velocity of this system also implies a small ejecta mass and slow pulsar kick (Dall'Osso et al. 2014).

ACKNOWLEDGEMENTS

We thank A. Wongwathanarat, M. Tanaka and T. Moriya for discussions. We also appreciate comments on an earlier draft of this paper by E. Müller, T. Piran, T. Tauris, and A. Tutukov. YS thanks the Max Planck Institute for Astrophysics for its hospitality. Numerical computations in this study were in part carried out on XC30 at CfCA in NAOJ and SR16000 at YITP in Kyoto University. YS was supported by Japan Society for the Promotion of Science (JSPS) postdoctoral fellowships for research abroad. KT was supported by research fellowships of JSPS for Young Scientists. This study was also supported in part by the Grant-in-Aid for Scientific Research (Nos. 24244028, 26400220 and 26400271), MEXT SPIRE, and JICFuS.

REFERENCES

- Abadie J., Abbott B. P., Abbott R., et al., 2010, *Classical and Quantum Gravity*, 27, 17, 173001
- Arnett W. D., 1982, *ApJ*, 253, 785
- Baron E., Cooperstein J., 1990, *ApJ*, 353, 597
- Bethe H. A., Wilson J. R., 1985, *ApJ*, 295, 14
- Bhattacharya D., van den Heuvel E. P. J., 1991, *Phys. Rep.*, 203, 1
- Blondin J. M., Mezzacappa A., DeMarino C., 2003, *ApJ*, 584, 971
- Bogomazov, A. I., Lipunov, V. M., & Tutukov, A. V. 2007, *Astronomy Reports*, 51, 308
- Brown G. E., Heger A., Langer N., Lee C.-H., Wellstein S., Bethe H. A. 2001, *New Astron.*, 6, 457
- Bruenn S. W., 1985, *ApJS*, 58, 771
- Bruenn S. W., Mezzacappa A., Hix W. R., et al., 2013, *ApJ*, 767, L6
- Buras R., Rampp M., Janka H.-T., Kifonidis K., 2006, *A&A*, 447, 1049
- Burrows A., 2013, *Reviews of Modern Physics*, 85, 245
- Colgate S. A., White R. H., 1966, *ApJ*, 143, 626
- Dall’Osso, S., Piran, T., & Shaviv, N. 2014, *MNRAS*, 438, 1005
- Dolence J. C., Burrows A., Zhang W., 2015, *ApJ*, 800, 10
- Drake A. J., Djorgovski S. G., Mahabal A., et al., 2009, *ApJ*, 696, 870
- Drout M. R., Chornock R., Soderberg A. M., et al., 2014, *ApJ*, 794, 23
- Drout M. R., Soderberg A. M., Gal-Yam A., et al., 2011, *ApJ*, 741, 97
- Drout M. R., Soderberg A. M., Mazzali P. A., et al., 2013, *ApJ*, 774, 58
- Foglizzo T., Kazeroni R., Guilet J., et al., 2015, *Publ. Astron. Soc. Australia*, 32, 9
- Hachinger S., Mazzali P. A., Taubenberger S., Hillebrandt W., Nomoto K., Sauer D. N., 2012, *MNRAS*, 422, 70
- Hanke, F., Müller, B., Wongwathanarat, A., Marek, A., & Janka, H.-T. 2013, *ApJ*, 770, 66
- Herwig, F., 2000, *A&A*, 360, 952
- Janka H.-T., 2012, *Annual Review of Nuclear and Particle Science*, 62, 407
- Kaiser, N., Burgett, W., Chambers, K., et al. 2010, *Proc. SPIE*, 7733, 77330E
- Keller S. C., Schmidt B. P., Bessell M. S., et al., 2007, *Publ. Astron. Soc. Australia*, 24, 1
- Kitaura F. S., Janka H., Hillebrandt W., 2006, *A&A*, 450, 345
- Kotake K., Takiwaki T., Suwa Y., et al., 2012, *Advances in Astronomy*, 2012
- Lattimer J. M., 2012, *Annual Review of Nuclear and Particle Science*, 62, 485
- Lattimer J. M., Swesty F. D., 1991, *Nuclear Physics A*, 535, 331
- Law N. M., Kulkarni S. R., Dekany R. G., et al., 2009, *PASP*, 121, 1395
- Liebendörfer M., Whitehouse S. C., Fischer T., 2009, *ApJ*, 698, 1174
- Melson, T., Janka, H.-T., & Marek, A. 2015, *ApJ*, 801, L24
- Melson, T., Janka, H.-T., Bollig, R., et al. 2015, *ApJ*, 808, L42
- Miyazaki, S., Komiyama, Y., Nakaya, H., et al. 2012, *Proc. SPIE*, 8446, 84460Z
- Moriya T. J., Tominaga N., Langer N., Nomoto K., Blinnikov S. I., Sorokina E. I., 2014, *A&A*, 569, A57
- Nagataki S., Hashimoto M.-a., Sato K., Yamada S., 1997, *ApJ*, 486, 1026
- Nakamura, K., Takiwaki, T., Kuroda, T., & Kotake, K. 2014, *arXiv:1406.2415*
- O’Connor E., Ott C. D., 2011, *ApJ*, 730, 70
- O’Connor E., Ott C. D., 2013, *ApJ*, 762, 126
- Pejcha O., Thompson T. A., 2015, *ApJ*, 801, 90
- Piran T., Shaviv N. J., 2005, *Physical Review Letters*, 94, 5, 051102
- Podsiadlowski, P., Langer, N., Poelarends, A. J. T., et al. 2004, *ApJ*, 612, 1044
- Rau A., Kulkarni S. R., Law N. M., et al., 2009, *PASP*, 121, 1334
- Scheck, L., Kifonidis, K., Janka, H.-T., Müller, E. 2006, *A&A*, 457, 963
- Siess L., 2009, *A&A*, 497, 463
- Stone J. M., Norman M. L., 1992, *ApJS*, 80, 753
- Sukhbold T., Woosley S. E., 2014, *ApJ*, 783, 10
- Suwa Y., 2014, *PASJ*, 66, L1
- Suwa Y., Kotake K., Takiwaki T., Liebendörfer M., Sato K., 2011, *ApJ*, 738, 165
- Suwa Y., Kotake K., Takiwaki T., Whitehouse S. C., Liebendörfer M., Sato K., 2010, *PASJ*, 62, L49
- Suwa Y., Takiwaki T., Kotake K., Fischer T., Liebendörfer M., Sato K., 2013, *ApJ*, 764, 99
- Suwa, Y., Yamada, S., Takiwaki, T., & Kotake, K. 2014, *arXiv:1406.6414*
- Takahashi K., Yoshida T., Umeda H., 2013, *ApJ*, 771, 28
- Takiwaki, T., Kotake, K., & Suwa, Y. 2014, *ApJ*, 786, 83
- Tauris T. M., Langer N., Moriya T. J., Podsiadlowski P., Yoon S.-C., Blinnikov S. I., 2013, *ApJ*, 778, L23
- Tauris, T. M., Langer, N., & Podsiadlowski, P. 2015, *MNRAS*, 451, 2123
- Timmes F. X., Woosley S. E., Weaver T. A., 1996, *ApJ*, 457, 834
- Tominaga N., Morokuma T., Tanaka M., et al., 2014, *The Astronomer’s Telegram*, 6291, 1
- Ugliano M., Janka H.-T., Marek A., Arcones A., 2012, *ApJ*, 757, 69
- Umeda H., Yoshida T., Takahashi K., 2012, *Progress of Theoretical and Experimental Physics*, 2012, 1, 01A302
- Wellstein S., Langer N. 1999, *A&A*, 350, 148
- Wongwathanarat, A., Janka, H.-T., Müller, E. 2013, *A&A*, 552, A126
- Woosley, S. E., & Heger, A. 2015, *arXiv:1505.06712*
- Yoshida T., Okita S., Umeda H., 2014, *MNRAS*, 438, 3119